Modulated Connection Modes of Redox Units in Molecular Junction Covalent Organic Framework for Artificial Photosynthetic Overall Reaction

Qi Li,[a],⊥ Jia-Nan Chang,[b],⊥ Zeng-Mei Wang,*,[a] Meng Lu,[b] Can Guo,[b] Mi Zhang,[b] Tao-Yuan Yu,[c] Yifa Chen,*,[b] Shun-Li Li[b] and Ya-Qian Lan*,[b]

[a]Jiangsu Key Laboratory of Construction Materials, College of Materials Science and Engineering, Southeast University, Nanjing 211189, P. R. China

[b]School of Chemistry, South China Normal University Guangzhou, 510006, P. R. China.

[c]Jiangsu Collaborative Innovation Centre of Biomedical Functional Materials, Jiangsu Key Laboratory of New Power Batteries, School of Chemistry and Materials Science, Nanjing Normal University, Nanjing 210023, PR China.

⊥Qi Li and Jia-Nan Chang contributed equally to this work.

KEYWORDS: Covalent organic framework; Redox molecular junction; Artificial Photosynthetic Overall Reaction; Charge transfer

ABSTRACT: The precise tuning of components, spatial orientations or connection modes for redox units is vital for gaining deep insight into efficient artificial photosynthetic overall reaction, yet it is still hard to be achieved for heterojunction photocatalysts. Here, we have developed a series of redox molecular junction covalent-organic-frameworks (COFs) (**M-TTCOF-Zn, M = Bi, Tri and Tetra**) for artificial photosynthetic overall reaction. The covalent connection between TAPP-Zn and multi-dentate TTF endows various connection-modes between water photo-oxidation (multi-dentate TTF) and CO_2 photo-reduction (TAPP-Zn) centers that can serve as desired platforms to study the possible interactions between redox centers. Notably, **Bi-TTCOF-Zn** exhibits a high CO production-rate of 11.56 μmol g^{-1} h^{-1} (selectivity, ~100%), which is more than 2 and 6 times higher than that of **Tri-TTCOF-Zn** and **Tetra-TTCOF-Zn**, respectively. As revealed by theoretical calculations, **Bi-TTCOF-Zn** facilitates more uniform distribution of energy-level orbitals, faster charge-transfer and stronger *OH adsorption/stabilization ability than that of **Tri-TTCOF-Zn** and **Tetra-TTCOF-Zn**.

INTRODUCTION

Over the past decades, the over-exploitation of fossil fuels has led to excessive CO_2 emission, causing for advanced technologies that can converse CO_2 into valuable products to realize the "loop closing" of CO_2 utilization.[1-4] Artificial photosynthetic overall reaction that mimics plants has attracted unprecedented interest due to its possibility in the conversion of CO_2 into value-added products like CO, HCOOH, CH_4 or methanol with the assistance of light energy and water.[5-7] In general, the artificial photosynthetic overall reaction contains simultaneously occurred CO_2 photo-reduction and water photo-oxidation, in which these two varied half reactions are coupled to achieve the overall reaction efficiency.[8] In this regard, it is essential yet still challenging to design efficient photocatalysts that endow these two half-reactions to be accomplished effectively due to the multi-requirements of photocatalysts (*e.g.*, light-absorption, charge separation/transfer, active sites for both CO_2 photo-reduction and water photo-oxidation, *etc.*)[9-11] that would need specific design of structure and functionality. In addition, the water photo-oxidation process, a vital half reaction to be balanced with CO_2 photo-reduction, has been generally neglected and received less attention.[12-14] Thus, the exploration of novel photocatalysts that can meet the multi-requirements of artificial photosynthetic overall reaction to provide deep insight into the possible interaction between the redox half reactions is of paramount importance.

In general, heterojunction photocatalysts with the characteristics of electron-hole separation efficiency and redox capability have been commonly investigated in artificial photosynthesis (Scheme 1a).[15-18] However, they are still difficult in precise tuning the components, spatial orientations or connection modes of redox units owing to their shortage in well-defined crystalline structures. Covalent organic frameworks (COFs), composed of lightweight elements (*e.g.*, carbon, nitrogen, oxygen, borane, *etc.*) *via* covalent bonds, are a promising class of porous crystalline materials with ordered pore structure and large surface area.[19-22] Attributed to the advantages, they hold much promise in potential applications of light energy triggered conversion reactions[23-25] and are

considered as desired alternatives for artificial photosynthetic overall reaction owing to the following reasons: i) the specially designed photo-sensitive organic struts can impart COFs with light absorption ability; ii) COFs with diverse functions can be easily modulated through in-situ design or post modification that might meet the multi-requirements of artificial photosynthetic overall reaction and iii) the well-defined pore structure of COFs can provide pre-organized pathways for efficient charge separation and transfer.[8, 26-28] To date, although a series of COFs have been applied in artificial photosynthetic overall reaction, most of them are based on the usage of sacrificial agents (*e.g.*, triethanolamine (TEOA), triisopropanolamine (TIPA)) or photosensitizers and only a few cases (*e.g.*, ACOF-1, N_3-COF, TTCOF-Zn or sp^2c-COF_{dpy}-Co, *etc.*)[29, 30] have been applied for artificial photosynthetic overall reaction using water as the electron donor. Nevertheless, their applications are still at the early stage[31-33] and generally suffer from the following bottlenecks: i) relatively low CO_2 catalytic conversion or product generation efficiency; ii) short in the charge transfer study that is much beneficial for improving the kinetic of artificial photosynthetic overall reaction; iii) lack in the modulation of components, spatial orientations or connection modes of redox units. Thus, it would be much interesting to design molecular junction COFs based platforms to conquer these bottlenecks and study the possible interactions between CO_2 photo-reduction and water photo-oxidation centers for artificial photosynthetic overall reaction. In particular, redox molecular junction COFs systems can inhibit the photogenerated charge recombination more effectively and enhance the photocatalytic performance largely when compared with the traditional heterojunction models.[34, 35] With these considerations in mind, we propose to select metalloporphyrin and multi-dentate tetrathiofulvalenyl (TTF) ligands to construct target COFs platforms, in which metalloporphyrin ligands are known to possess good visible-light absorption and CO_2 photo-activation ability,[36] while TTF has shown superior role in water photo-oxidation (Scheme 1b).[37, 38] If multi-dentate (i.e. 2, 3, or 4-dentate) TTF can be connected with metalloporphyrin units, it would provide a series of desired structure platforms with different connection modes to gain deep insight into artificial photosynthetic overall reaction, yet such powerful systems are still challenging and rare as far as we know.

As a proof-of-concept, a series of multi-dentate TTF based COFs (i.e., **Bi-TTCOF-Zn**, **Tri-TTCOF-Zn** and **Tetra-TTCOF-Zn**) have been prepared as desired platforms to investigate the artificial photosynthetic overall reaction (Scheme 1). The covalent connection between TAPP-Zn and multi-dentate TTF promotes the electron transfer from multi-dentate TTF to TAPP-Zn, thus-obtained photo-excited electrons (on TAPP-Zn) and holes (on TTF) can be utilized for CO_2 photo-reduction and water photo-oxidation, respectively. Notably, best of them, **Bi-TTCOF-Zn** exhibits a superior CO production rate of 11.56 μmol g^{-1} h^{-1} (selectivity, ~100%), which is more than 2 and 6 times higher than that of **Tri-TTCOF-Zn** and **Tetra-TTCOF-Zn**, respectively. As revealed by theoretical calculations, **Bi-TTCOF-Zn** facilitates the more uniform distribution of HOMO and LUMO orbitals, faster charge transfer and stronger *OH adsorption/stabilization ability than that of **Tri-TTCOF-Zn** and **Tetra-TTCOF-Zn**. This work might promote the deep understanding the artificial photosynthetic overall reaction.

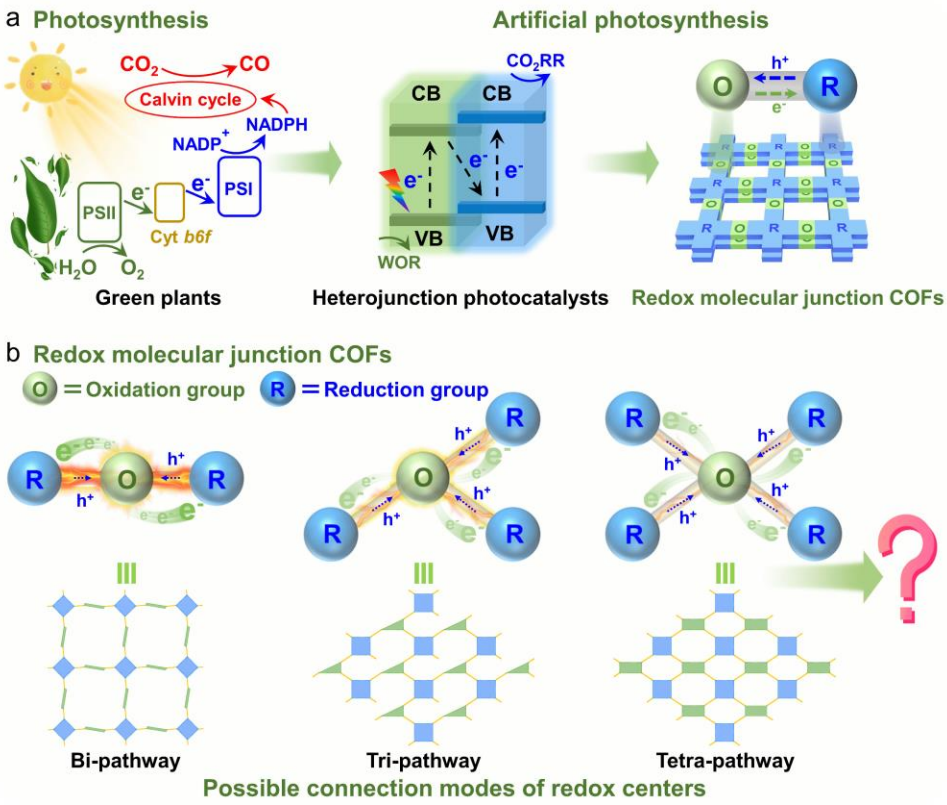

Scheme 1. Schematic representation of the possible connection modes of redox molecular junction COFs for artificial photosynthetic overall reaction. (a) The photosynthesis inspired artificial photosynthesis by heterojunction photocatalysts and redox molecular junction COFs. (b) Redox molecular junction COFs with possible connection modes.

RESULTS AND DISCUSSION

Synthesis and structure of M-TTCOF-Zn. M-TTCOF-Zn (M = Bi, Tri or Tetra) were synthesized by Schiff-base condensation between Zn-coordinated 5,10,15,20-tetrakis(4-aminophenyl)porphyrin (TAPP-Zn) and 2, 6-bi (4-formylphenyl) tetrathiafulvalene (Bi-TTF), 2, 3, 6-tri (4-formylphenyl) tetrathiafulvalene (Tri-TTF) and 2, 3, 6, 7-tetra (4-formylphenyl) tetrathiafulvalene (Tetra-TTF) by solvothermal methods (details see Methods). The crystalline structures of **M-TTCOF-Zn (M = Bi, Tri or Tetra)** have been confirmed by the powder X-ray diffraction (PXRD) analyses combined with the theoretical simulated calculations using Materials Studio software package (Figure 1).[39] On the basis of theoretical structural simulation and Pawley refinements, the **Bi-TTCOF-Zn** can be fitted into the AB stacking model with the corresponding unit cell parameters of $a = b = 35.8149$ Å, $c = 6.4938$ Å, and $\alpha = \beta = \gamma = 90°$ in the $I4$ space group (Table S1). As revealed by the differential plot, the refinement of PXRD pattern is well agreement with the experimental one (unweighted-profile R factor (R_p), 3.02% and weighted profile R factor (R_{wp}), 4.40%), suggesting the validity of the computational model (Figure 1b). **Bi-TTCOF-Zn** displays intense PXRD peaks at 5.04, 7.09, 10.09 and 13.96, which can be assigned to the (200), (220), (400) and (101) facets, respectively (Figure 1b and Table S1). The simulated crystal structure of **Bi-TTCOF-Zn** shows an 1D channel along the c axis with a theoretical pore size of 1.16 nm and the adjacent stacking distance is detected to be 3.29 Å (Figure 1a). Furthermore, the structures of **Tri-TTCOF-Zn** and **Tetra-TTCOF-Zn** have also been analyzed through the similar procedures (Figure 1c and 1d). The results show that **Tri-TTCOF-Zn** is fitted into *PM* space group with unit cell parameters of $a = 20.6675$ Å, $b = 3.5430$ Å, and $c = 26.4910$ Å, $\alpha = \beta = \gamma = 90°$ (R_p, 1.20%; R_{wp}, 1.63%) (Table S2). For **Tetra-TTCOF-Zn**, it can be classified into *P222* space group with unit cell parameters of $a = 29.0104$ Å, $b = 19.7675$ Å, and $c = 3.6830$ Å, $\alpha = \beta = \gamma = 90°$ (R_p, 3.81; R_{wp}, 3.95), which is similar to that of reported works (Figure 1c, d and Table S3).[37] Thus, we have successfully prepared three kinds of **M-TTCOF-Zn (M = Bi, Tri or Tetra)** for further characterizations.

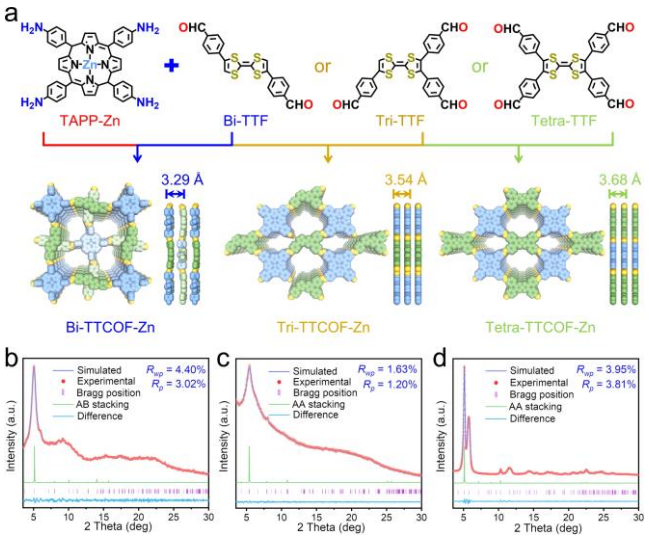

Figure 1. The structure and characterization of **M-TTCOF-Zn (M = Bi, Tri or Tetra)**. (a) The structures of **M-TTCOF-Zn (M = Bi, Tri or Tetra)**. (b), (c) and (d) Experimental (red dot) and simulated (blue line) PXRD patterns of **Bi-TTCOF-Zn** (b), **Tri-TTCOF-Zn** (c) and **Tetra-TTCOF-Zn** (d).

In addition, the Fourier transform infrared (FT-IR) spectroscopy have been applied to study the chemical compositions of **M-TTCOF-Zn (M = Bi, Tri or Tetra)**. Taking **Bi-TTCOF-Zn** for instance, the C=N stretching vibration band at 1621 cm^{-1} appears in the FT-IR measurements, suggesting the successful formation of C=N bonds (Figure 2a). Meanwhile, this result can be further certified by the obviously decreased -CHO stretching vibration band (1699 cm^{-1}) and -NH_2 vibration band (3205 and 3500 cm^{-1}) for the reactant monomers.[40] Similar results have also been detected for **Tri-TTCOF-Zn** and **Tetra-TTCOF-Zn** (Figure S1). Besides, the characteristic peak at 160.1 ppm (i.e., g) in ^{13}C solid-state NMR spectroscopy (^{13}C ssNMR) is fitted into the carbon atom of the C=N bond for **Bi-TTCOF-Zn**, proving the existence of convent bonding. Meanwhile, other detected peaks can be assigned to the related carbon atoms for porphyrin (i.e., a, b and c), phenyl (i.e., d, e, f and h) and Bi-TTF (i.e., i) units (Figure 2b).[34, 37, 41, 42] In addition, X-ray photoelectron spectroscopy (XPS) analysis has been carried out to investigate the divalent state of Zn in **M-TTCOF-Zn (M = Bi, Tri or Tetra)** (Figures S2-S5).[40, 43, 44] For the XPS spectra of **Bi-TTCOF-Zn**, four main peaks with binding energy of 1021.70, 164.10, 284.80 and 399.68 eV are ascribed to Zn 2p, S 2p, C 1s and N 1s, respectively (Figure S3). In the S 2p region, two kinds of peaks with binding energy of 163.90 eV (S 2p3/2) and 165.29 eV (S 2p1/2) can be attributed to the characteristic peaks of C-S bond in Bi-TTF unit (Figure S3). Moreover, the observed binding energy values of 1021.70 eV and 1044.70 eV belong to the Zn $2p_{3/2}$ and Zn $2p_{1/2}$ for **Bi-TTCOF-Zn**, respectively (Figure S3). Similar results have also been detected for **Tri-TTCOF-Zn** and **Tetra-TTCOF-Zn** (Figures S4 and S5). Specifically, the Zn content in **Bi-TTCOF-Zn**, **Tri-TTCOF-Zn** and **Tetra-TTCOF-Zn** are determined to be 3.77 wt%, 4.62 wt% and 4.15 wt% by inductively coupled plasma (ICP) optical emission spectrometry (Table S4). Additionally, metal-free **Bi-TTCOF-2H** has also been prepared and characterized with PXRD and XPS tests that can serve as a contrast sample to **M-TTCOF-Zn (M = Bi, Tri or Tetra)** (Figures S6 and S7).

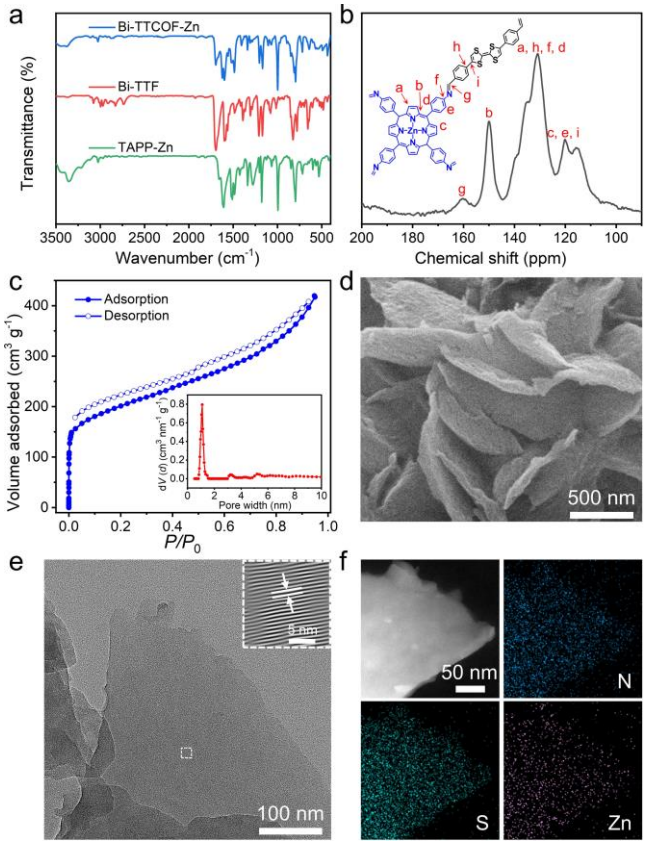

Figure 2. Characterizations of **Bi-TTCOF-Zn**. (a) FT-IR spectra of **Bi-TTCOF-Zn.** (b) ^{13}C ssNMR spectrum of **Bi-TTCOF-Zn.** (c) N_2 sorption curves of **Bi-TTCOF-Zn** at 77 K. (d) SEM image of **Bi-TTCOF-Zn.** (e) TEM image of **Bi-TTCOF-Zn** (inset is the Fourier transform image of the HRTEM for the circled place). (f) EDS elemental mapping images of **Bi-TTCOF-Zn**.

The surface area and porosity of **M-TTCOF-Zn (M = Bi, Tri or Tetra)** have been evaluated by N_2 sorption tests at 77 K (Figure 2c and Figures S8 and S9). In detail, the Brunauer-Emmett-Teller surface area (S_{BET}) of **Bi-TTCOF-Zn**, **Tri-TTCOF-Zn** and **Tetra-TTCOF-Zn** are calculated to be 716 $m^2 g^{-1}$, 459 $m^2 g^{-1}$ and 587 $m^2 g^{-1}$, respectively. Taking **Bi-TTCOF-Zn** for example, its pore size distribution centers at ~1.1 nm, which basically complies with the theoretical value in the structure (Figure 2c).[45] The N_2 sorption tests of **Bi-TTCOF-2H** has also been performed, showing a slightly lower S_{BET} (271 $m^2 g^{-1}$) than that of **Bi-TTCOF-Zn** (Figure S10). Moreover, the chemical stability of **Bi-TTCOF-Zn** has been examined by immersing it into different solvents at room temperature. The almost identical PXRD patterns and FT-IR spectra when compared with the state before test prove its high structural stability (Figures S11 and S12). Additionally, the thermal stability of **M-TTCOF-Zn (M = Bi, Tri or Tetra)** has also been confirmed by the thermogravimetric analysis,

in which all of them can be stable up to ~300 °C (Figures S13-S15).

Furthermore, the scanning electron microscopy (SEM) and transmission electron microscopy (TEM) tests have been conducted to reveal the morphology of these samples.[46] **Bi-TTCOF-Zn** displays a kind of nanosheet morphology (Figure 2d, e). Specifically, the oriented lattice fringes of **Bi-TTCOF-Zn** are clearly visible and the detected lattice spacing of 1.28 nm can be ascribed to the (2 2 0) plane in the high-resolution TEM (HR-TEM) image, proving the high crystallinity of **Bi-TTCOF-Zn** (inset image, Figure 2e). Additionally, energy-dispersive X-ray spectroscopy (EDS) elemental mapping images reveal that C, N, S, and Zn are uniformly distributed in **Bi-TTCOF-Zn** (Figure 2f). Besides, the morphology of **Tri-TTCOF-Zn** and **Tetra-TTCOF-Zn** has also been characterized by SEM and TEM tests (Figures S16 and S17).

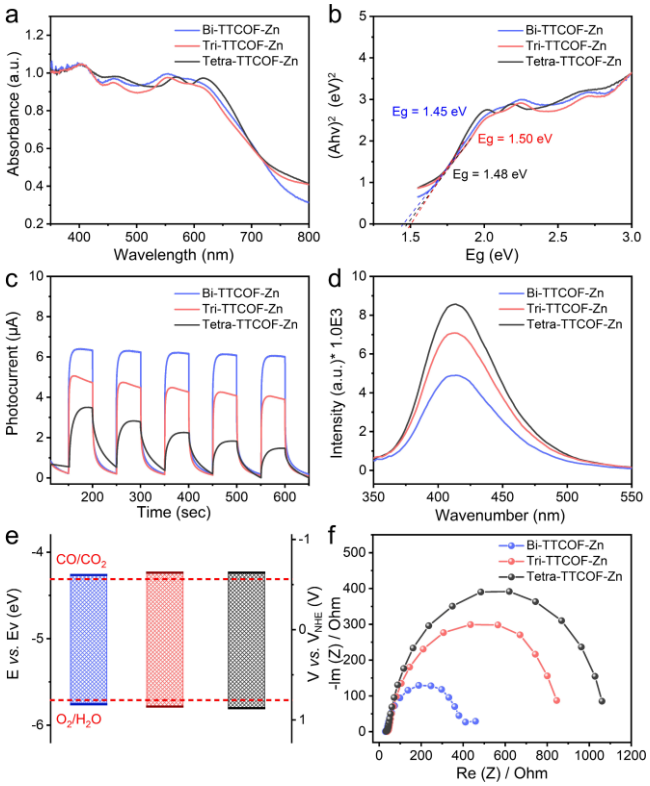

Figure 3. Characterizations of the optical properties for **Bi-TTCOF-Zn**, **Tri-TTCOF-Zn** and **Tetra-TTCOF-Zn**. (a) UV/Vis absorption spectra. (b) Tauc plot for band gap calculation. (c) Transient photocurrent response. (d) PL spectra. (e) Band-structure diagrams of **Bi-TTCOF-Zn** (blue), **Tri-TTCOF-Zn** (red) and **Tetra-TTCOF-Zn** (black). (f) Nyquist plots.

To study the artificial photosynthetic overall reaction, CO_2 adsorption ability is an important factor for the photocatalysts. Hence, the CO_2 adsorption tests have been performed at 298 K and their adsorption capacity are calculated to be 62, 40, and 48 $cm^3\ g^{-1}$ for **Bi-TTCOF-Zn**, **Tri-TTCOF-Zn** and **Tetra-TTCOF-Zn**, respectively, implying the high affinity to CO_2 (Figures S18-S20). These results are also supported by the CO_2 temperature programmed desorption (TPD) tests (Figures S21). Specifically, the adsorption capacity of **Bi-TTCOF-Zn** is two times higher than that of **Bi-TTCOF-2H** (28 $cm^3\ g^{-1}$, Figure S22), indicating the strong interaction between TAPP-Zn unit and CO_2 molecule.

Photocatalytic performances of samples.

In general, to accomplish the artificial photosynthetic overall reaction, the basic requirements of photocatalyst need a more negative conduction band minimum (CBM) potential than that of CO_2 photo-reduction (CO/CO_2, theoretically -0.53 V vs. NHE, pH 7 and -4.37 eV *vs.* E_v, vacuum level) and meanwhile a more positive valence band maximum (VBM) potential than that of water photo-oxidation (O_2/H_2O, theoretically 0.82 V *vs.* NHE, pH 7 and -5.67 eV *vs.* E_v).[47] In this regard, UV/Vis diffuse reflectance spectroscopy (DRS) and ultraviolet photoelectron spectroscopy (UPS) have performed to determine the optical properties of **M-TTCOF-Zn (M = Bi, Tri or Tetra)**. Based on the test results, they all display wide absorption range and the related band gaps (Eg) are calculated to be 1.45, 1.48, and 1.50 eV for **Bi-TTCOF-Zn**, **Tri-TTCOF-Zn** and **Tetra-TTCOF-Zn** by Tauc plots (Figure 3a, 3b and Figures S23-S25), respectively.[34, 44, 48] In addition, the intensity of transient photocurrent response of **Bi-TTCOF-Zn** is much higher than **Tri-TTCOF-Zn** and **Tetra-TTCOF-Zn**, which implies that the covalent connection between Bi-TTF and TAPP-Zn can result in higher photo-induced charge separation and transfer efficiency (Figure 3c).Moreover, the VBM of **Bi-TTCOF-Zn** is determined to be -5.68 eV (*vs.* E_v) from the UPS spectrum (Figure S23) and the CBM is thus calculated to be -4.23 eV (*vs.* E_v), suggesting its ability to accomplish the artificial photosynthetic overall reaction. In addition to these, Mott-Schottky measurements have also been carried out to investigate the band positions of **M-TTCOF-Zn (M = Bi, Tri or Tetra)** (Figure 3e and Figures S23-S25) and the results comply with the UPS tests. Furthermore, **Bi-TTCOF-2H** has also been characterized by the similar methods (Figure S26) and its related energy-band results are showed in Figure S27. In addition, photoluminescence (PL) has been performed to study the charge separation behaviour. The PL intensity of **Bi-TTCOF-Zn** is significantly quenched when compared with that of **Tri-TTCOF-Zn** and **Tetra-TTCOF-Zn** (Figure 3d).[52] In addition, the surface photovoltage spectra (SPV) (Figure S28) and transient photovoltage (TPV) (Figure S29) tests reveal the better charge separation ability of **Bi-TTCOF-Zn** than that of **Tri-TTCOF-Zn** and **Tetra-TTCOF-Zn.**[48, 49] Moreover, the electrochemical impedance spectroscopy (EIS) has been tested to study the charge transfer resistance (Figure 3f). Notably, the Nyquist plots of **Bi-TTCOF-Zn** present a much smaller charge transfer resistance than that of **Tri-TTCOF-Zn** and **Tetra-TTCOF-Zn**, which can further prove its better charge transfer ability.

Based on above mentioned results, we further set out to explore the performance of artificial photosynthetic overall reaction. The visible light-driven (420 - 800 nm) artificial photosynthetic overall reaction is performed under pure CO_2 (1.0 atm, 298 K) atmosphere in CO_2-saturated H_2O solution without any additional photosensitizer or sacrificial agent (Figure S30). During the tests, each data point is calculated based on three separate trials under similar conditions to give the average one and apply error bar to reflect the standard deviation of the tests. For **Bi-TTCOF-Zn**, its time-dependent CO output increases almost linearly with the irradiation time (Figure S31). Based on the basic evaluation of the performance, **Bi-TTCOF-Zn** shows a CO production rate of 11.56 μmol g^{-1} h^{-1} at 24 h, which is higher than that of **Tri-TTCOF-Zn** (4.28 μmol g^{-1} h^{-1}) and **Tetra-TTCOF-Zn** (1.75 μmol g^{-1} h^{-1}) (Figure 4a). In contrast, TAPP-Zn monomer shows negligible reaction activity (0.094 μmol g^{-1} h^{-1}) (Figure 4a). Besides, no activity has been detected for **Bi-TTCOF-2H**. At the same time, the CO and O_2 production amounts are 32.9 ± 2.2 μmol and 17.0 ± 1.3 μmol in a 24 h batch experiment, respectively. The CO/O_2 yield ratio is calculated to be about 2:1 for **Bi-TTCOF-Zn**, which basically complies with the reaction modes of the artificial photosynthetic overall reaction (Figure 4b). Similar results have also been detected for **Tri-TTCOF-Zn** and **Tetra-TTCOF-Zn**, revealing their suitable band structures for artificial photosynthetic overall reaction (Figure 4b).

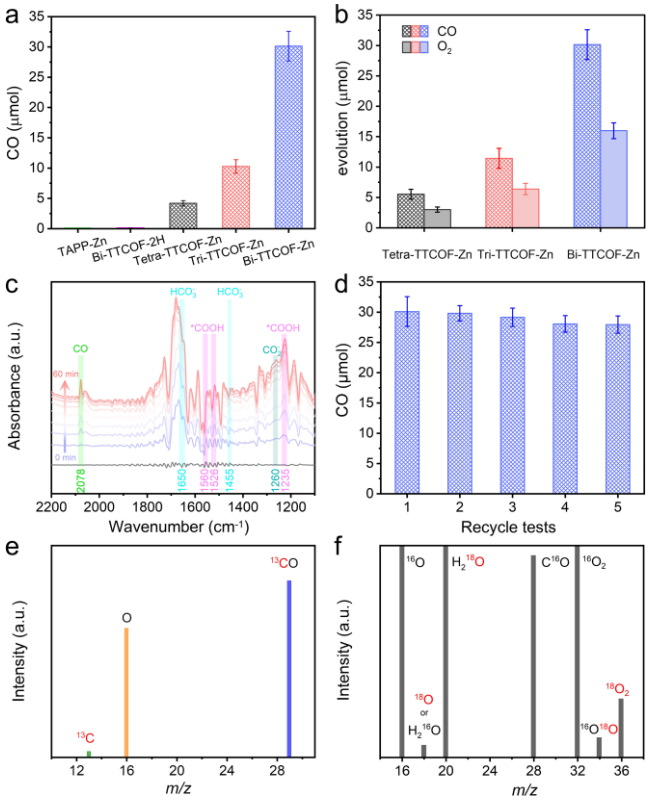

Figure 4. Photocatalytic performances of samples. (a) Photocatalytic CO_2-to-CO performance of Bi-TTF, TAPP-Zn and **M-TTCOF-Zn (M = Bi, Tri or Tetra)**. (b) The evolution of CO and O_2 detected on an online system after 24 h for **M-TTCOF-Zn (M = Bi, Tri or Tetra)**. (c) DRIFTs spectrum of **Bi-TTCOF-Zn** in CO_2-to-CO process (the dark line represents the baseline). (d) Cycling performance of **Bi-TTCOF-Zn**. (e) MS of ^{13}CO (m/z = 29) produced from the photocatalytic reduction of $^{13}CO_2$. (f) $^{18}O_2$ isotope experiment result to explore the source of O_2.

To study the possible intermediates generated during the photocatalytic process, in situ diffuse reflectance infrared Fourier transform spectroscopy (DRIFTs) has been performed and **Bi-TTCOF-Zn** with the optimal property is selected as the target sample. After adding **Bi-TTCOF-Zn** into the reaction system for 30 min under dark condition, bicarbonate (HCO_3^- at 1650 and 1455 cm^{-1}) can be detected as a result of the CO_2 adsorption (Figure 4c). Under visible-light illumination, the observed peaks at 1560, 1526 and 1235 cm^{-1} are in accordance with the asymmetric stretching vibrations of *COOH. Besides, the band of 1260 cm^{-1} can be assigned to the adsorbed CO_2^- (Figure 4c).[50, 51] Additionally, the isotope labelling experiments have been carried out to investigate the carbon and oxygen sources of the products. $^{13}CO_2$ has been initially applied as the substrate and ^{13}CO (m/z = 29) is thus detected in the mass spectrometry (MS) of product, which verifies the source of CO (Figure 4e). Furthermore, $^{18}O_2$ (m/z = 36) and $^{18}O^{16}O$ (m/z = 34) can be monitored in the gas phase when $H_2{}^{18}O$ is used as the reaction solution (Figure 4f), certifying that the produced $^{18}O_2$ indeed stems from the photo-oxidation of $H_2{}^{18}O$. In general, the recycling stability is also a vital parameter to evaluate the durability of photocatalyst. Notably, the performance of **Bi-TTCOF-Zn** can remain almost intact for at least five cycles with unchanged component, crystallinity and structure during the recycling tests as verified by PXRD, FT-IR and XPS tests (Figure 4d and Figures S32-S34).[52]

To gain deep insight into the possible mechanism, density function theory calculations have been introduced to discuss the possible influence factors. The apparent performance can be composed by two factors, namely, the light absorption efficiency and the catalytic activity. We will discuss these issues respectively in the following. The first is the light absorption efficiency. For **M-TTCOF-Zn (M = Bi, Tri or Tetra)**, it can be seen from Figure 5a that the simulated absorbance spectra of all the three samples possess the absorption peaks among the range from 350 to 800 nm. Remarkably, the **Bi-TTCOF-Zn** has the strongest absorbance intensity and therefore the highest photon excitation efficiency, which is consistent to the above-mentioned SPV results. Nevertheless, there exists minor inconsistency when compared the simulated absorbance spectra with DRS tests, which could stem from the depletion of photons in the region < 500 nm that in turn hinders the complete utilization of potential transition modes as predicted by time-dependent density functional theory (TDDFT) (Figures S35-S37). Thus, the strongest absorbance intensity might be one of the reasons that **Bi-TTCOF-Zn** outperforms **Tri-TTCOF-Zn** and **Tetra-TTCOF-Zn**. Then, for the highest occupied molecular

orbital (HOMO) and lowest unoccupied molecular orbital (LUMO) distributions, the HOMO and LUMO orbitals of the **Bi-TTCOF-Zn** are more uniformly distributed, both at the TAPP-Zn and Bi-TTF (Figure S38). For **Tri-TTCOF-Zn** and **Tetra-TTCOF-Zn**, the distribution is more localized, with HOMO mainly on the TAPP-Zn, and LUMO mainly on the Tri- or Tetra-TTF. Such a uniform distribution property makes the light absorbance intensity is stronger on **Bi-TTCOF-Zn** that would enhance the number of accessible sites. This is another reason to support the superior performance of **Bi-TTCOF-Zn** to **Tri-TTCOF-Zn** and **Tetra-TTCOF-Zn** (Figure S38).

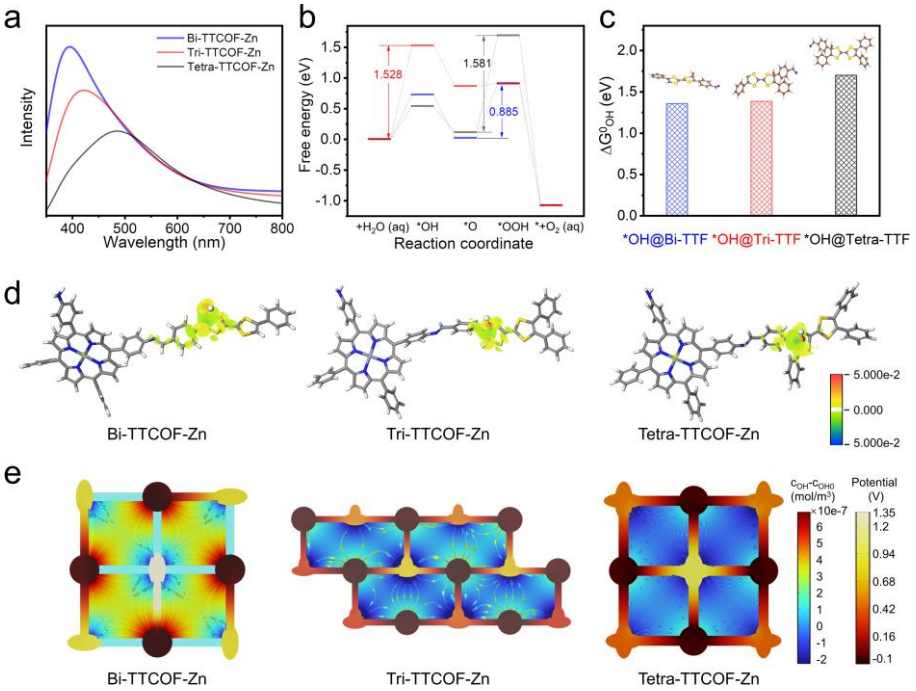

Figure 5. Theoretical calcualtions of **M-TTCOF-Zn (M = Bi, Tri or Tetra)** in artificial photosynthetic overall reaction. (a) The calculated absorption spectrums for **M-TTCOF-Zn (M = Bi, Tri or Tetra)**. (b) Water photo-oxidation free energy diagram (the potential is taken as 1.5 V *vs* RHE; blue, **Bi-TTCOF-Zn;** red, **Tri-TTCOF-Zn;** dark, **Tetra-TTCOF-Zn**). (c) Comparison of the adsorption energy of *OH on **M-TTCOF-Zn (M = Bi, Tri or Tetra)** (the value is defined as the Gibbs energy of reaction $H_2O \rightarrow *OH + H^+ + e$ at 1.5 V *vs* RHE, the lower value indicates the stronger adsorption). (d) The charge density difference after the adsorption of *OH. (e) The variation of OH^- concentration and diffusion direction on the **M-TTCOF-Zn (M = Bi, Tri or Tetra)** obtained by FEM simulation (the c_{OH} is shown by colormap, and the diffusion direction is shown by streamlines, the dark colored circle represents the TAPP-Zn unit and the light-colored ellipse stands for TTF units).

Except for the light absorption efficiency, the catalytic activity is also an important factor to assess the related performance. To investigate it, the free energy diagrams (FED) of the associated reactions of water photo-oxidation (for HOMO) and CO_2 photo-reduction (for LUMO) are calculated (*via* computational hydrogen electrode method) (Figure 5b and Figure S39).[53] In general, the reaction centers are chosen by the sites with the largest occupations of HOMO/LUMO orbitals.[54] We find that the HOMO reaction mainly takes place at TTF, while LUMO reaction mainly takes place at the TAPP-Zn (Figure S38). Specifically, the LUMO reaction (CO_2 photo-reduction) shows a similar ΔG_{max} of 1.24 eV for **M-TTCOF-Zn (M = Bi, Tri or Tetra)** (Figure S39), possibly due to their similar TAPP-Zn units and minor effect of different multi-dentate TTF on the ΔG values for the CO_2 photo-reduction process. Meanwhile, the HOMO reactions present ΔG_{max} of 0.885, 1.528 and 1.581 eV for **Bi-TTCOF-Zn**, **Tri-TTCOF-Zn** and **Tetra-TTCOF-Zn**, respectively (Figure 5b and Figure S40). It is worth noting that although the HOMO reactions of **M-TTCOF-Zn (M = Bi, Tri or Tetra)** occur at multi-dentate (i.e., 2, 3, or 4-dentate) TTF, the different connection modes of **M-TTCOF-Zn (M = Bi, Tri or Tetra)** lead to differences in their photocatalytic performances (Figure 5b).

Moreover, we also compare the adsorption energies for the formation of *OH (a vital rate determining step intermediate for water photo-oxidation process) on Bi-TTF, Tri-TTF and Tetra-TTF units for **M-TTCOF-Zn (M = Bi, Tri or Tetra)**, respectively (Figure 5c). For these three different TTF units, they display varied numbers of unoccupied C sites by phenyl group in addition to the similar TTF host, in which there are two, one and none unoccupied C sites for Bi-TTF, Tri-TTF and Tetra-TTF units, respectively. According to the previous work from Markovic et al,[55] the unoccupied C sites by phenyl group will indicate a benefit in proton donation, which then favours the performance improvement. Specifically, based on our calculation, the *OH adsorption energy on the unoccupied C site is much larger than that of S site in TTF (Figure S41), thus the number of unoccupied C sites would play a significant effect on the interaction with *OH. In this regard, **Bi-TTCOF-Zn** would exhibit the largest oxophilicity with *OH. As proved by the differential charge

densities, it can be seen that adsorption on C(H) for **Bi-TTCOF-Zn** leads to a larger charge density rearrangement than that of **Tri-TTCOF-Zn** and **Tetra-TTCOF-Zn** (Figure 5d).

After understanding the characteristics of this reaction, we have further performed the finite elemental method simulations to modulate the properties of intermediate or product diffusion in the reaction (Figure 5e). Based on the reaction of photogenerated electrodes, we set *OH consumption at the photogenerated anode (TTF unit) and production at the photogenerated cathode (TAPP unit) and simulate its transport direction based on the finite elemental method simulations. The difference in the concentration gradient of OH^- can be seen according to the degree of non-uniformity of the colormap in the cavity. Specifically, in **M-TTCOF-Zn (M = Bi, Tri or Tetra)**, **Bi-TTCOF-Zn** has the highest non-uniformity, indicating that the OH^- concentration gradient in its cavity is the largest, i.e., the most OH^- is produced. Besides, from the number of streamlines, the order of photocurrent magnitude is **Bi-TTCOF-Zn** > **Tri-TTCOF-Zn** > **Tetra-TTCOF-Zn**, and correspondingly, the order of c_{OH} concentration polarization in space is **Bi-TTCOF-Zn** > **Tri-TTCOF-Zn** > **Tetra-TTCOF-Zn**, and the same is true for the photocurrent (Figure S42 and Videos S1-S3). In addition, the transport direction of CO diffuses from the cavity to the direction outside the vertical paper surface (Figure S43). The concentration changes of c_{CO} follow the similar order (Figure S43 and Videos S4-S6). In view of these, we can see that the potentials obtained for these three photocatalysts are different due to the different light absorption efficiencies, in which the order is **Bi-TTCOF-Zn** > **Tri-TTCOF-Zn** > **Tetra-TTCOF-Zn** (Figure 5e). Finally, we made an animation of the changes of c_{OH} and c_{CO} in the whole process to show the photocatalytic process more graphically (Videos S1-S6).

CONCLUSIONs

In summary, we have synthesized a series of redox molecular junction COFs (**M-TTCOF-Zn, M = Bi, Tri and Tetra**) that can serve as desired platforms to study the interactions between water photo-oxidation and CO_2 photo-reduction centers in artificial photosynthetic overall reaction. Specifically, the covalent connection between TAPP-Zn and multi-dentate TTF within **M-TTCOF-Zn (M = Bi, Tri or Tetra)** endows various connection modes between water photo-oxidation (multi-dentate TTF) and CO_2 photo-reduction (TAPP-Zn) centers. Best of them, **Bi-TTCOF-Zn** exhibits a high CO production rate of 11.56 $\mu mol\ g^{-1}\ h^{-1}$ (selectivity, ~100%), which is more than 2 and 6 times higher than that of **Tri-TTCOF-Zn** and **Tetra-TTCOF-Zn**, respectively. Combined theoretical calculations with experiments, **Bi-TTCOF-Zn** facilitates the more uniform distribution HOMO and LUMO orbitals, faster charge transfer and stronger *OH adsorption/stabilization ability than that of **Tri-TTCOF-Zn** and **Tetra-TTCOF-Zn**. This work might facilitate the development of redox crystalline photocatalysts for the understanding of structure-function relationship in artificial photosynthetic overall reaction.

ASSOCIATED CONTENT

Supporting Information. Detailed information regarding the experimental methods, characterization analysis, DFT calculations, simulation for theoretical COF structures. This material is available free of charge via the Internet at http://pubs.acs.org.

AUTHOR INFORMATION

Corresponding Author

Ya-Qian Lan.

* yqlan@m.scnu.edu.cn
Homepage: http://www.yqlangroup.com

Zeng-Mei Wang.

* 101011338@seu.edu.cn

Yifa Chen.

* chyf927821@163.com

Author Contributions

Q. L. and J.-N. C. contributed equally to this work.

Notes

The authors declare no competing financial interest.

ACKNOWLEDGMENT

This work was financially supported by the NSFC (Grants 51978153, 22225109, 22071109 and 22171139). Natural Science Foundation of Guangdong Province (No. 2023B1515020076).

REFERENCES

(1) Davies, T. W.; Smyth, T., Why artificial light at night should be a focus for global change research in the 21st century. *Global Change Biol.,* **2018,** *24* (3), 872-882.

(2) Li, X.; Yu, J.; Jaroniec, M.; Chen, X., Cocatalysts for Selective Photoreduction of CO_2 into Solar Fuels. *Chem. Rev.,* **2019,** *119* (6), 3962-4179.

(3) Banerjee, T.; Podjaski, F.; Kröger, J.; Biswal, B. P.; Lotsch, B. V., Polymer photocatalysts for solar-to-chemical energy conversion. *Nat. Rev. Mater.,* **2021,** *6* (2), 168-190.

(4) Liang, Z.; Wang, H.-Y.; Zheng, H.; Zhang, W.; Cao, R., Porphyrin-based frameworks for oxygen electrocatalysis and catalytic reduction of carbon dioxide. *Chem. Soc. Rev.,* **2021,** *50* (4), 2540-2581.

(5) Yu, J.; Huang, L.; Tang, Q.; Yu, S.-B.; Qi, Q.-Y.; Zhang, J.; Ma, D.; Lei, Y.; Su, J.; Song, Y.; Eloi, J.-C.; Harniman, R. L.; Borucu, U.; Zhang, L.; Zhu, M.; Tian, F.; Du, L.; Phillips, D. L.; Manners, I.; Ye, R.; Tian, J., Artificial spherical chromatophore nanomicelles for selective CO_2 reduction in water. *Nat. Catal.,* **2023,** *6* (6), 464-475.

(6) Barber, J., Photosynthetic energy conversion: natural and artificial. *Chem. Soc. Rev.,* **2009,** *38* (1), 185-196.

(7) Marzo, L.; Pagire, S. K.; Reiser, O.; König, B., Visible-Light Photocatalysis: Does It Make a Difference in Organic Synthesis? *Angew. Chem. Int. Ed.,* **2018,** *57* (32), 10034-10072.

(8) Kosco, J.; Moruzzi, F.; Willner, B.; McCulloch, I., Photocatalysts Based on Organic Semiconductors with Tunable Energy Levels for Solar Fuel Applications. *Adv. Energy Mater.,* **2020,** *10* (39), 2001935.

(9) Geng, K.; He, T.; Liu, R.; Dalapati, S.; Tan, K. T.; Li, Z.; Tao, S.; Gong, Y.; Jiang, Q.; Jiang, D., Covalent Organic Frameworks: Design, Synthesis, and Functions. *Chem. Rev.,* **2020,** *120* (16), 8814-8933.
(10) Lu, M.; Zhang, M.; Liu, J.; Chen, Y.; Liao, J.-P.; Yang, M.-Y.; Cai, Y.-P.; Li, S.-L.; Lan, Y.-Q., Covalent Organic Framework Based Functional Materials: Important Catalysts for Efficient CO_2 Utilization. *Angew. Chem. Int. Ed.,* **2022,** *61* (15), e202200003.
(11) Yoshino, S.; Takayama, T.; Yamaguchi, Y.; Iwase, A.; Kudo, A., CO_2 Reduction Using Water as an Electron Donor over Heterogeneous Photocatalysts Aiming at Artificial Photosynthesis. *Acc. Chem. Res.,* **2022,** 55 (7), 966-977.
(12) Zhang, G.; Lan, Z.-A.; Wang, X., Surface engineering of graphitic carbon nitride polymers with cocatalysts for photocatalytic overall water splitting. *Chem. Sci.,* **2017,** *8* (8), 5261-5274.
(13) Sarkar, P.; Chowdhury, I. H.; Das, S.; Islam, S. M., Recent trends in covalent organic frameworks (COFs) for carbon dioxide reduction. *Mater. Adv.,* **2022,** *3* (22), 8063-8080.
(14) Alemán, J.; Mas-Ballesté, R., Photocatalytic Oxidation Reactions Mediated by Covalent Organic Frameworks and Related Extended Organic Materials. *Front. Chem.,* **2021,** *9*, 708312.
(15) Wang, Q.; Warnan, J.; Rodríguez-Jiménez, S.; Leung, J. J.; Kalathil, S.; Andrei, V.; Domen, K.; Reisner, E., Molecularly engineered photocatalyst sheet for scalable solar formate production from carbon dioxide and water. *Nat. Energy,* **2020,** *5* (9), 703-710.
(16) Jiang, Y.; Liao, J.-F.; Chen, H.-Y.; Zhang, H.-H.; Li, J.-Y.; Wang, X.-D.; Kuang, D.-B., All-Solid-State Z-Scheme α-Fe_2O_3/Amine-RGO/$CsPbBr_3$ Hybrids for Visible-Light-Driven Photocatalytic CO_2 Reduction. *Chem,* **2020,** *6* (3), 766-780.
(17) Wang, Y.; Shang, X.; Shen, J.; Zhang, Z.; Wang, D.; Lin, J.; Wu, J. C. S.; Fu, X.; Wang, X.; Li, C., Direct and indirect Z-scheme heterostructure-coupled photosystem enabling cooperation of CO_2 reduction and H_2O oxidation. *Nat. Commun.,* **2020,** *11* (1), 3043.
(18) Xu, F.; Meng, K.; Cheng, B.; Wang, S.; Xu, J.; Yu, J., Unique S-scheme heterojunctions in self-assembled TiO_2/$CsPbBr_3$ hybrids for CO_2 photoreduction. *Nat. Commun.,* **2020,** *11* (1), 4613.
(19) Diercks, C. S.; Yaghi, O. M., The atom, the molecule, and the covalent organic framework. *Science,* **2017,** *355*, eaal1585.
(20) Jin, Y.; Hu, Y.; Zhang, W., Tessellated multiporous two-dimensional covalent organic frameworks. *Nat. Rev. Chem.,* **2017,** *1* (7), 0056.
(21) Waller, P. J.; Gándara, F.; Yaghi, O. M., Chemistry of Covalent Organic Frameworks. *Acc. Chem. Res.,* **2015,** *48* (12), 3053-3063.
(22) Wang, H.; Zeng, Z.; Xu, P.; Li, L.; Zeng, G.; Xiao, R.; Tang, Z.; Huang, D.; Tang, L.; Lai, C.; Jiang, D.; Liu, Y.; Yi, H.; Qin, L.; Ye, S.; Ren, X.; Tang, W., Recent progress in covalent organic framework thin films: fabrications, applications and perspectives. *Chem. Soc. Rev.,* **2019,** *48* (2), 488-516.
(23) Chen, J.; Tao, X.; Li, C.; Ma, Y.; Tao, L.; Zheng, D.; Zhu, J.; Li, H.; Li, R.; Yang, Q., Synthesis of bipyridine-based covalent organic frameworks for visible-light-driven photocatalytic water oxidation. *Appl. Catal. B Environ.,* **2020,** *262*, 118271.
(24) Song, Y.; Sun, Q.; Aguila, B.; Ma, S., Opportunities of Covalent Organic Frameworks for Advanced Applications. *Adv. Sci.,* **2019,** *6* (2), 1801410.
(25) Liu, R.; Tan, K. T.; Gong, Y.; Chen, Y.; Li, Z.; Xie, S.; He, T.; Lu, Z.; Yang, H.; Jiang, D., Covalent organic frameworks: an ideal platform for designing ordered materials and advanced applications. *Chem. Soc. Rev.,* **2021,** *50* (1), 120-242.
(26) Zhou, Z.; Xiao, Y.; Tian, J.; Nan, N.; Song, R.; Li, J., Recent advances in metal-free covalent organic frameworks for photocatalytic applications in energy and environmental fields. *J. Mater. Chem. A,* **2023,** *11*, 3245-3261.
(27) Ran, L.; Li, Z.; Ran, B.; Cao, J.; Zhao, Y.; Shao, T.; Song, Y.; Leung, M. K. H.; Sun, L.; Hou, J., Engineering Single-Atom Active Sites on Covalent Organic Frameworks for Boosting CO_2 Photoreduction. *J. Am. Chem. Soc.,* **2022,** *144* (37), 17097-17109.
(28) Huang, N.; Wang, P.; Jiang, D., Covalent organic frameworks: a materials platform for structural and functional designs. *Nat. Rev. Mater.,* **2016,** *1* (10), 16068.
(29) Nguyen, H. L., Reticular Materials for Artificial Photoreduction of CO_2. *Adv. Energy Mater.,* **2020,** *10* (46), 2002091.
(30) Zhao, C.; Chen, Z.; Shi, R.; Yang, X.; Zhang, T., Recent Advances in Conjugated Polymers for Visible-Light-Driven Water Splitting. *Adv. Mater.,* **2020,** *32* (28), 1907296.
(31) Chen, H.; Jena, H. S.; Feng, X.; Leus, K.; Van Der Voort, P., Engineering Covalent Organic Frameworks as Heterogeneous Photocatalysts for Organic Transformations. *Angew. Chem. Int. Ed.,* **2022,** *61* (47), e202204938.
(32) Ding, S.-Y.; Wang, W., Covalent organic frameworks (COFs): from design to applications. *Chem. Soc. Rev.,* **2013,** *42* (2), 548-568.
(33) Heidary, N.; Harris, T. G. A. A.; Ly, K. H.; Kornienko, N., Artificial photosynthesis with metal and covalent organic frameworks (MOFs and COFs): challenges and prospects in fuel-forming electrocatalysis. *Physiol. Plantarum.,* **2019,** *166* (1), 460-471.
(34) Chang, J.-N.; Li, Q.; Shi, J.-W.; Zhang, M.; Zhang, L.; Li, S.; Chen, Y.; Li, S.-L.; Lan, Y.-Q., Oxidation-Reduction Molecular Junction Covalent Organic Frameworks for Full Reaction Photosynthesis of H_2O_2. *Angew. Chem. Int. Ed.,* **2023,** *62* (9), e202218868.
(35) Zhang, L.; Li, R.-H.; Li, X.-X.; Liu, J.; Guan, W.; Dong, L.-Z.; Li, S.-L.; Lan, Y.-Q., Molecular oxidation-reduction junctions for artificial photosynthetic overall reaction. *Proc. Natl. Acad. Sci. U.S.A.,* **2022,** *119* (40), e2210550119.
(36) Kojima, T.; Honda, T.; Ohkubo, K.; Shiro, M.; Kusukawa, T.; Fukuda, T.; Kobayashi, N.; Fukuzumi, S., A Discrete Supramolecular Conglomerate Composed of Two Saddle-Distorted Zinc(II)-Phthalocyanine Complexes and a Doubly Protonated Porphyrin with Saddle Distortion Undergoing Efficient Photoinduced Electron Transfer. *Angew. Chem. Int. Ed.,* **2008,** *47* (35), 6712-6716.
(37) Lu, M.; Liu, J.; Li, Q.; Zhang, M.; Liu, M.; Wang, J.-L.; Yuan, D.-Q.; Lan, Y.-Q., Rational Design of Crystalline Covalent Organic Frameworks for Efficient CO_2 Photoreduction with H_2O. *Angew. Chem. Int. Ed.,* **2019,** *58* (36), 12392-12397.
(38) Adeel, S. M.; Li, Q.; Nafady, A.; Zhao, C.; Siriwardana, A. I.; Bond, A. M.; Martin, L. L., A systematic study of the variation of tetrathiafulvalene (TTF), $TTF^{+\cdot}$ and TTF^{2+} reaction pathways with water in the presence and absence of light. *RSC. Adv.,* **2014,** *4* (91), 49789-49795.
(39) Lin, S.; Diercks, C. S.; Zhang, Y.-B.; Kornienko, N.; Nichols, E. M.; Zhao, Y.; Paris, A. R.; Kim, D.; Yang, P.; Yaghi, O. M.; Chang, C. J., Covalent organic frameworks comprising cobalt porphyrins for catalytic CO_2 reduction in water. *Science,* **2015,** *349* (6253), 1208-1213.
(40) Wu, Q.; Xie, R.-K.; Mao, M.-J.; Chai, G.-L.; Yi, J.-D.; Zhao, S.-S.; Huang, Y.-B.; Cao, R., Integration of Strong Electron Transporter Tetrathiafulvalene into Metalloporphyrin-Based Covalent Organic Framework for Highly Efficient Electroreduction of CO_2. *ACS Energy Lett.,* **2020,** *5* (3), 1005-1012.
(41) Yao, X.; Guo, C.; Song, C.; Lu, M.; Zhang, Y.; Zhou, J.; Ding, H.-M.; Chen, Y.; Li, S.-L.; Lan, Y.-Q., In Situ Interweaved High Sulfur Loading Li–S Cathode by Catalytically Active Metalloporphyrin Based Organic Polymer Binders. *Adv. Mater.,* **2023,** *35* (7), 2208846.
(42) Ding, S.-Y.; Gao, J.; Wang, Q.; Zhang, Y.; Song, W.-G.; Su, C.-Y.; Wang, W., Construction of Covalent Organic Framework for Catalysis: Pd/COF-LZU1 in Suzuki–Miyaura Coupling Reaction. *J. Am. Chem. Soc.,* **2011,** *133* (49), 19816-19822.
(43) Liu, M.; Wang, Y.-R.; Ding, H.-M.; Lu, M.; Gao, G.-K.; Dong, L.-Z.; Li, Q.; Chen, Y.; Li, S.-L.; Lan, Y.-Q., Self-assembly of anthraquinone covalent organic frameworks as 1D superstructures for highly efficient CO_2 electroreduction to CH_4. *Sci. Bull.,* **2021,** *66* (16), 1659-1668.
(44) Chang, J.-N.; Li, Q.; Yan, Y.; Shi, J.-W.; Zhou, J.; Lu, M.; Zhang, M.; Ding, H.-M.; Chen, Y.; Li, S.-L.; Lan, Y.-Q., Covalent-Bonding Oxidation Group and Titanium Cluster to Synthesize a Porous Crystalline Catalyst for Selective Photo-Oxidation Biomass Valorization. *Angew. Chem. Int. Ed.,* **2022,** *61* (37), e202209289.

(45) Jiang, C.; Zhang, Y.; Zhang, M.; Ma, N.-N.; Gao, G.-K.; Wang, J.-H.; Zhang, M.-M.; Chen, Y.; Li, S.-L.; Lan, Y.-Q., Exfoliation of covalent organic frameworks into MnO_2-loaded ultrathin nanosheets as efficient cathode catalysts for Li-CO_2 batteries. *Cell. Rep. Phys. Sci.,* **2021,** *2* (4), 100392.
(46) Lee, M. K.; Shokouhimehr, M.; Kim, S. Y.; Jang, H. W., Two-Dimensional Metal–Organic Frameworks and Covalent–Organic Frameworks for Electrocatalysis: Distinct Merits by the Reduced Dimension. *Adv. Energy Mater.,* **2022,** *12* (4), 2003990.
(47) Liu, X.; Inagaki, S.; Gong, J., Heterogeneous Molecular Systems for Photocatalytic CO_2 Reduction with Water Oxidation. *Angew. Chem. Int. Ed.,* **2016,** 55 (48), 14924-14950.
(48) Yang, J.; Jing, J.; Li, W.; Zhu, Y., Electron Donor–Acceptor Interface of TPPS/PDI Boosting Charge Transfer for Efficient Photocatalytic Hydrogen Evolution. *Adv. Sci.,* **2022,** *9* (17), 2201134.
(49) Liu, T.; Zhu, W.; Wang, N.; Zhang, K.; Wen, X.; Xing, Y.; Li, Y., Preparation of Structure Vacancy Defect Modified Diatomic-Layered g-C_3N_4 Nanosheet with Enhanced Photocatalytic Performance. *Adv. Sci.,* **2023,** *10* (24), 2302503.
(50) Zhao, X.; Xu, M.; Song, X.; Zhou, W.; Liu, X.; Yan, Y.; Huo, P., Charge separation and transfer activated by covalent bond in UiO-66-NH_2/RGO heterostructure for CO_2 photoreduction. *Chem. Eng. J.,* **2022,** *437*, 135210.
(51) Zhou, J.; Li, J.; Kan, L.; Zhang, L.; Huang, Q.; Yan, Y.; Chen, Y.; Liu, J.; Li, S.-L.; Lan, Y.-Q., Linking oxidative and reductive clusters to prepare crystalline porous catalysts for photocatalytic CO_2 reduction with H_2O. *Nat. Commun.,* **2022,** *13* (1), 4681.
(52) Zhang, K.; Kirlikovali, K. O.; Varma, R. S.; Jin, Z.; Jang, H. W.; Farha, O. K.; Shokouhimehr, M., Covalent Organic Frameworks: Emerging Organic Solid Materials for Energy and Electrochemical Applications. *ACS Appl. Mater. Interfaces,* **2020,** *12* (25), 27821-27852.
(53) Nørskov, J. K.; Rossmeisl, J.; Logadottir, A.; Lindqvist, L.; Kitchin, J. R.; Bligaard, T.; Jónsson, H., Origin of the Overpotential for Oxygen Reduction at a Fuel-Cell Cathode. *J. Phys. Chem. B,* **2004,** *108* (46), 17886-17892.
(54) Huang, Q.; Liu, J.; Feng, L.; Wang, Q.; Guan, W.; Dong, L.-Z.; Zhang, L.; Yan, L.-K.; Lan, Y.-Q.; Zhou, H.-C., Multielectron transportation of polyoxometalate-grafted metalloporphyrin coordination frameworks for selective CO_2-to-CH_4 photoconversion. *Nat. Sci. Rev.,* **2019,** *7* (1), 53-63.
(55) Strmcnik, D.; Uchimura, M.; Wang, C.; Subbaraman, R.; Danilovic, N.; van der Vliet, D.; Paulikas, A. P.; Stamenkovic, V. R.; Markovic, N. M., Improving the hydrogen oxidation reaction rate by promotion of hydroxyl adsorption. *Nat. Chem.,* **2013,** 5 (4), 300-306.